



Short communication

SiO₂/Cu/polyacrylonitrile-C composite as anode material in lithium ion batteries

Mingqi Li, Jing Li, Kai Li, Yan Zhao, Yongguang Zhang, Denise Gosselink, P. Chen*

Department of Chemical Engineering, University of Waterloo, Waterloo, N2L3G1 Canada



HIGHLIGHTS

- A SiO₂/Cu/PAN-C composite anode is synthesized of CuO-coated SiO₂ and polyacrylonitrile.
- The composite exhibits good cyclic stability and rate capability with a high reversible capacity.
- The composite improves conductivity and reduces volume change of active material during cycling.

ARTICLE INFO

Article history:

Received 1 December 2012

Received in revised form

6 May 2013

Accepted 9 May 2013

Available online 17 May 2013

Keywords:

SiO₂/Cu/PAN-C

Composite

Anode

Lithium ion battery

Electrochemical performance

ABSTRACT

A new SiO₂/Cu/polyacrylonitrile-C composite (denoted as SiO₂/Cu/PAN-C) is prepared by mechanical ball milling and heat treatment of CuO-coated SiO₂ and polyacrylonitrile. During heat treatment, Cu is produced by reduction of CuO and SiO₂ is embedded in the matrix of Cu and PAN-C. SiO₂ in the composite presents a specific capacity of 1230 mAh g⁻¹, and exhibits excellent cyclic stability and rate capability when cycling in the voltage range of 0.0–3.0 V. Electrochemical impedance spectra (EIS) indicate that the addition of Cu effectively improves the conductivity of electrode and diminishes interfacial impedance.

© 2013 Elsevier B.V. All rights reserved.

1. Introduction

Development of safe, low cost, high capacity, stable cycle performance and environmentally friendly electrode materials for lithium ion batteries is essential for applications in portable electronic devices and electric vehicles. To this end, a large number of studies have been conducted [1–11]. Among anode materials, Si is considered a very promising candidate for next-generation lithium batteries due to high specific capacity and abundant resources, but a large volume change (about 300%) during cycling results in poor cyclic stability, hindering its applications [12,13]. In recent years, the pulverization of Si particles has been largely overcome by designing special nanostructures, such as nanoparticles, nanowires, nanotubes, and nanoporous structures [14–18]. However, the practical application of these

materials still faces many challenges. Firstly, they are accompanied with some intrinsic drawbacks like a high cost, low packing density and serious surface side-reactions. Secondly, although the pulverization of single Si particle is solved in these materials, with increasing the loaded active materials on per unit area, the microstructure of the electrode is still easily destroyed in a prolonged cycling [17,19]. Additionally, in order to decrease the volume change during cycling, enhancing the discharge cut-off voltage or limiting the charge capacity was widely adopted during the electrochemical performance measurement of silicon electrodes. These techniques can significantly improve the cyclic performance of silicon-based electrode in a half cell, but they meet challenges in full batteries with Si anodes [20]. Firstly, because the potential polarization degree of cathode in full batteries varies during cycling and the potential difference of forming different Li_xSi alloys is very tiny, it is very difficult to accurately control the lithium-insertion depth of Si by limiting cut-off voltage in a full battery. Secondly, limiting charge capacity in a full battery easily causes a low first coulombic efficiency and a slow dynamic of

* Corresponding author.

E-mail address: p4chen@uwaterloo.ca (P. Chen).

Li-ion diffusion during lithium insertion into Si from the second cycle because a part of lithium ion always remains in Si while the lithium ion in the cathode is limited.

Comparatively, although having a specific capacity lower than that of Si, silicon oxides have a less volume change during cycling and the first lithiation process results in the formation of nano-sized amorphous Si clusters surrounded by lithium oxides and lithium silicates that act as buffer layers to accommodate the volume change during cycling. The use of silicon oxides may provide an improved cycling performance. Many studies have demonstrated that SiO composites exhibit much better cycle performance than Si composites [21–23]. Recently, it was found that another silicon oxide, SiO_2 , could also react with lithium with a high specific capacity. For example, Guo et al. reported that the reversible capacity of $\text{SiO}_2/\text{hard carbon}$ composite is $\sim 630 \text{ mAh g}^{-1}$, in which SiO_2 delivers a reversible lithium storage capacity of 1675 mAh g^{-1} [24]. Yu et al. indicated that a C– SiO_2 composite with 50.1% SiO_2 delivered an initial discharge capacity of 536 mAh g^{-1} [21]. Since SiO_2 has much lower cost and is more abundant than Si or SiO, and its volume change during cycling is the least among silicon-based materials, it is a very promising alternative material. However, low electronic conductivity is the biggest handicap for SiO_2 to be used as an electrode material.

To our knowledge, there are only limited reports devoted to electrochemical behavior of SiO_2 as an anode for lithium batteries. In this work, a new $\text{SiO}_2/\text{Cu}/\text{PAN-C}$ composite is prepared by a simple method. Here, in order to improve the conductivity of SiO_2 electrode, Cu is introduced into the composite material by reduction of CuO. PAN-C is chosen as a dispersive matrix for SiO_2 because of its good conductivity and effective buffering to the volume change of the active material [25]. In addition, PAN can dissolve in NMP but is insoluble in ethanol, which helps to get a uniformly PAN-coated SiO_2 precursor by precipitation in our experiments.

2. Experimental

2.1. Preparation of $\text{SiO}_2/\text{Cu}/\text{PAN-C}$

Preparation of CuO-coated SiO_2 : 0.9613 g of $\text{Cu}(\text{NO}_3)_2 \cdot 3\text{H}_2\text{O}$ (Sigma) was dissolved in deionized water with continuous stirring. Subsequently, 1 g of SiO_2 porous spheres (5–15 nm in diameter, Sigma) was dispersed in the solution with the help of sonication. And then, water was evaporated at 100°C to give $\text{Cu}(\text{NO}_3)_2$ -coated SiO_2 solid mixture. The mixture was treated at 200°C in air for 3 h to form the CuO-coated SiO_2 composite.

Preparation of $\text{SiO}_2/\text{Cu}/\text{PAN-C}$: 1.3056 g of PAN (Sigma) was dissolved in 10 mL of N-methylpyrrolidinone (NMP). 0.8 g of CuO-coated SiO_2 and the PAN solution were batched in a zirconium dioxide vial. In order to homogeneously disperse SiO_2 in the PAN matrix, the mixture was subjected to mechanical milling in a high energy ball mill (Pulverisette7, Germany), up to 36 h at a speed of 600 rpm using zirconium dioxide balls of 5 mm diameter, with a ball to powder weight ratio of 10:1. After ball milling, ethanol was added into the solution to precipitate PAN-coated SiO_2/CuO composite. Subsequently, the PAN-coated SiO_2/CuO composite was transferred to a tube furnace. The furnace was heated to 1000°C from room temperature at a rate of $10^\circ\text{C min}^{-1}$ under an argon atmosphere with a flow rate of 100 mL min^{-1} , and then was kept at 1000°C for 3 h. The obtained product was further milled for 2 h at a speed of 500 rpm in an argon atmosphere. In order to understand the effect of Cu on the electrochemical properties of the resultant material, $\text{SiO}_2/\text{PAN-C}$ composite with the same SiO_2 percentage was also synthesized using a similar preparation method.

2.2. Materials characterization

To identify the phase constitution, the resultant composites were characterized by X-ray diffraction (XRD, D8 Discover, Bruker) employing $\text{Cu K}\alpha$ ($\lambda = 0.15406 \text{ nm}$) radiation at a scan rate of $2.5^\circ \text{ min}^{-1}$ from 10° to 90° . Thermogravimetric analysis (TGA, TA 2960, TA Instrument) was performed for composite materials to determine the ratio of different ingredients. The TGA experiments were carried out in air at a heating rate of 3 K min^{-1} . Scanning electron microscopy (SEM, Leo-1530, Zeiss) and energy dispersive X-ray image maps (EDX-map) were conducted to investigate the morphology, microstructure and element distribution of the as-prepared composites. Fourier-transform infrared reflection (FTIR) spectra were recorded on a vertex 70 FTIR spectrometer for further confirming the composition of the as-prepared composites. The specific surface area was determined by the Brunauer–Emmet–Teller method (BET, ASAP 2020, Micromeritics).

2.3. Electrochemical measurement

The electrochemical performance of the as-prepared SiO_2 composite materials was evaluated using 2032 coin cells assembled in an argon-filled glove box. Working electrodes were fabricated by painting slurry with 80 wt% of active material powder, 5 wt% of acetylene black (AB) and 15 wt% of carboxymethyl cellulose (CMC) onto Ni foam ($\sim 1.5 \text{ cm}^2$). The resulting film was dried at 100°C in vacuum for 12 h. The loaded total mass of active material was $\sim 4\text{--}5 \text{ mg}$ (not containing AB and CMC). A lithium disc was used as the counter electrode and reference electrode. The electrolyte was 1 M LiPF_6 dissolved in a mixed solvent of ethylene carbonate (EC) and dimethyl carbonate (DMC) (1:1 in weight) with 2% vinylene carbonate (VC) added to improve the cycling stability of electrode. Cells were cycled in the voltage range of $0.0\text{--}3.0 \text{ V}$ with different current density. Cyclic voltammetry (CV) was carried out in the potential range of $0.0\text{--}3.0 \text{ V}$ at a scan rate of 0.1 mV s^{-1} on EC-Lab (Biologic Science Instruments). After cell charging was over, EIS measurements were performed at open circuit potential with an alternate current amplitude of 10 mV over the frequency range from 100 k to 0.01 Hz .

3. Results and discussion

Fig. 1(a) shows the XRD profiles of SiO_2 , $\text{SiO}_2/\text{PAN-C}$ and $\text{SiO}_2/\text{Cu}/\text{PAN-C}$. Two broad and weak peaks appear at 23.5° and 42.8° in the XRD pattern of pristine SiO_2 , revealing a mainly amorphous nature of the structure. After coating by PAN-C, only a new broad and weak peak at 22° , which corresponds to the (0 0 2) plane of carbon, is observed in the XRD of $\text{SiO}_2/\text{PAN-C}$, indicating that no other new crystalline products such as SiC and Si are formed and PAN-C is also amorphous. Compared with the XRD of $\text{SiO}_2/\text{PAN-C}$, three new sharp peaks located at 43.4° , 50.5° and 74.5° present in the XRD pattern of $\text{SiO}_2/\text{Cu}/\text{PAN-C}$, which are assigned to the (1 1 1), (2 0 0) and (2 2 0) lattice planes of element Cu (PDF# 04-0836, cubic cell, $a = b = c = 3.61$), respectively, confirming CuO was successively reduced to element Cu by PAN-C during heat treatment.

The FTIR spectra of SiO_2 , $\text{SiO}_2/\text{PAN-C}$ and $\text{SiO}_2/\text{Cu}/\text{PAN-C}$ are shown in **Fig. 1(b)**. There are three characteristic peaks attributed to SiO_2 . Compared to crystalline SiO_2 , a red shift of the frequency assigned to asymmetry Si–O–Si bond stretching and O–Si–O bond deformation occurs, which shift from 1102 cm^{-1} to 1064 cm^{-1} and from 472 cm^{-1} to 447 cm^{-1} , respectively, while the peak attributed to SiO_4 tetrahedron ring (798 cm^{-1}) has no obvious shift. The red shift phenomenon due to amorphization was also observed by Liu et al., in which the Si–O stretching peak of the amorphous state shifts to a lower position [26]. This result agrees well with our

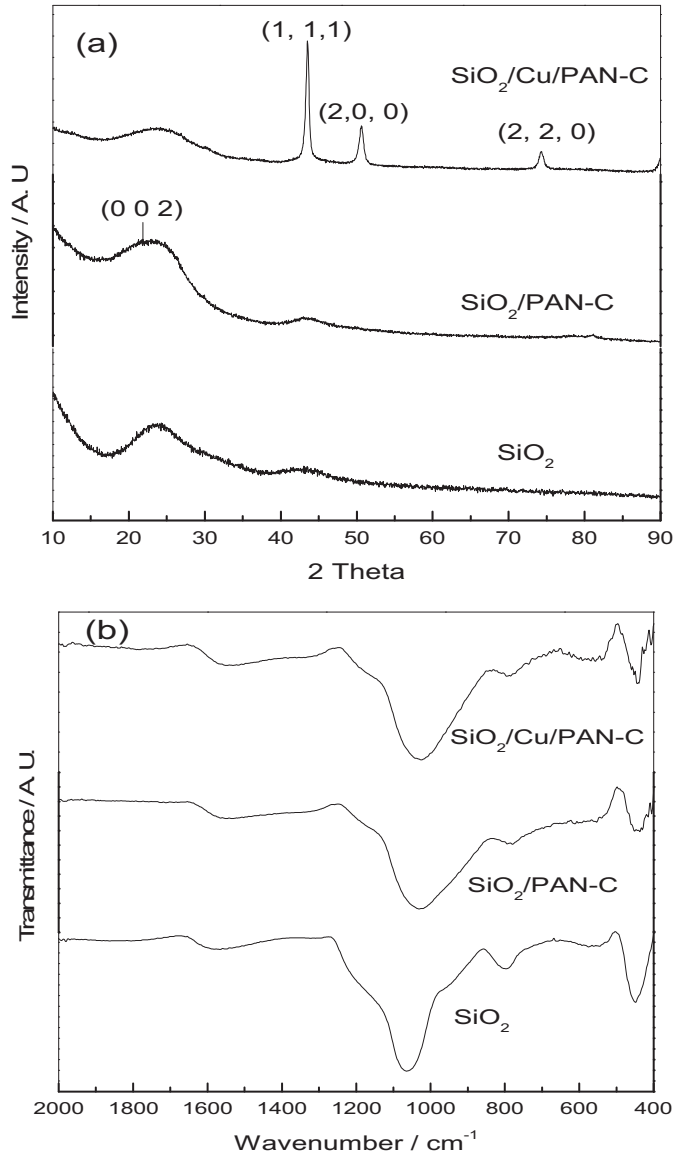


Fig. 1. XRD patterns (a) and FT-IR spectra (b) of pristine SiO_2 , $\text{SiO}_2/\text{PAN-C}$ and $\text{SiO}_2/\text{Cu}/\text{PAN-C}$.

results. After milling and coating by PAN-C, all characteristic peaks attributed to SiO_2 become weak and no new peak is observed, suggesting there is no reaction between SiO_2 and C. The FTIR of $\text{SiO}_2/\text{Cu}/\text{PAN-C}$ does not show obvious difference by comparison to $\text{SiO}_2/\text{PAN-C}$, indicating copper exists in composite material with elemental form.

Fig. 2 is the thermogravimetric analysis profiles of $\text{SiO}_2/\text{PAN-C}$ (a) and $\text{SiO}_2/\text{Cu}/\text{PAN-C}$ (b). Based on the TG analysis and stoichiometry in our experiments, SiO_2 , Cu and PAN-C in the $\text{SiO}_2/\text{Cu}/\text{PAN-C}$ composite account for about ~40 wt%, ~7 wt% and ~53 wt %, respectively, while SiO_2 and PAN-C in the $\text{SiO}_2/\text{PAN-C}$ composite are ~40 wt% and ~60 wt %, respectively. Compared with $\text{SiO}_2/\text{PAN-C}$, the TG and DTA analysis curves of $\text{SiO}_2/\text{Cu}/\text{PAN-C}$ display some significant differences. The total mass of $\text{SiO}_2/\text{Cu}/\text{PAN-C}$ gradually increases in the range of 150–300 °C, corresponding to the oxidation of element Cu. In addition, the combustion temperature of partial PAN-C rises to 650 °C, resulting from a different chemical environment because a part of carbon might be coated by copper film. After Cu is oxidized to CuO during heating in air, the thermal conductivity becomes poor.

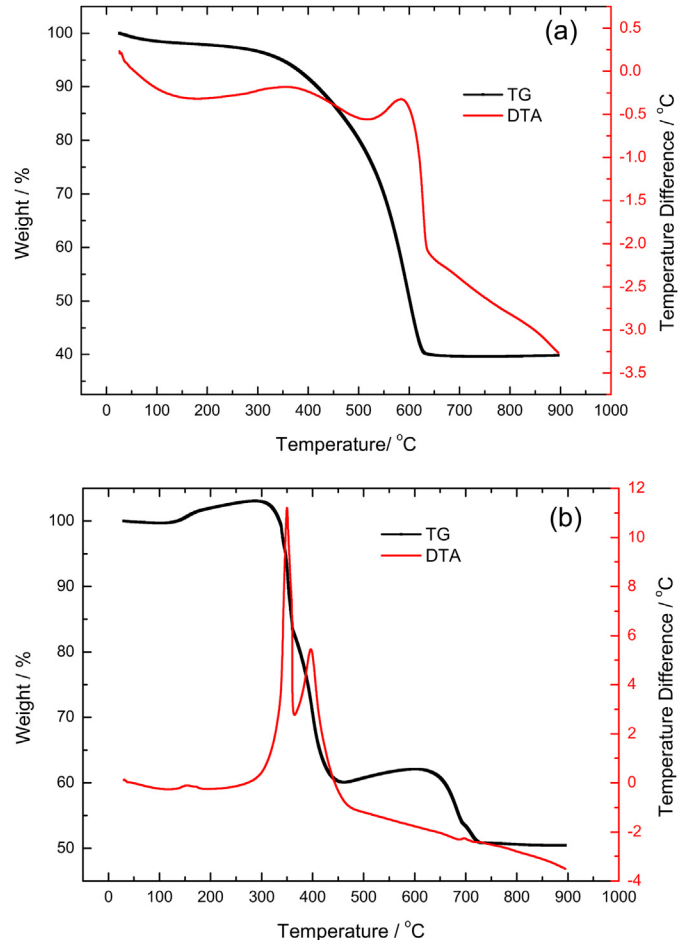


Fig. 2. Thermogravimetric analysis curves of $\text{SiO}_2/\text{PAN-C}$ (a) and $\text{SiO}_2/\text{Cu}/\text{PAN-C}$ (b).

Fig. 3 shows the SEM images of the pure SiO_2 , $\text{SiO}_2/\text{PAN-C}$ and $\text{SiO}_2/\text{Cu}/\text{PAN-C}$, and the EDX elemental mapping analysis of $\text{SiO}_2/\text{Cu}/\text{PAN-C}$. The diameter of the pure SiO_2 particles is about 5–15 nm (Sigma). After heat treatment, SiO_2 particles are coated by PAN-C with some big blocks (Fig. 3(b)). With the addition of Cu and the decrease of PAN-C, the particle size of $\text{SiO}_2/\text{Cu}/\text{PAN-C}$ decreases and its size distribution becomes narrow, which is advantageous to improve its electrochemical performance. Elemental mapping was used here to evaluate the distribution uniformity of C, O, Si and Cu in the $\text{SiO}_2/\text{Cu}/\text{PAN-C}$ composite. It is clear that C, O and Si are distributed uniformly in the composite, while Cu presents a relatively low dispersion degree in the composite because it is mainly located at the space between C and SiO_2 .

The porosities of $\text{SiO}_2/\text{PAN-C}$ and $\text{SiO}_2/\text{Cu}/\text{PAN-C}$ were characterized by BET measurement (Fig. 4). Two composites present a clear hysteresis between adsorption and desorption at high relative pressures and thus indicate that they contain mesopores (2–50 nm) [27]. After the relative pressure increases to 0.8, the absorbed quantity rises sharply, suggesting there are macropores, which may come from the aggregates of primary particles during milling. Barrett–Joyner–Halenda (BJH) adsorption curve indicates the pore diameter of two composites have a wide distribution. Large amounts of micropores may arise from PAN pyrolysis. The average pore size of $\text{SiO}_2/\text{PAN-C}$ and $\text{SiO}_2/\text{Cu}/\text{PAN-C}$ is about 64 nm and 79 nm, respectively. A bigger average pore size of $\text{SiO}_2/\text{Cu}/\text{PAN-C}$ results from the reduction of CuO by PAN-C, leaving some voids. Because the insertion of Cu into PAN-C decreases the porosity, the pore volumes of $\text{SiO}_2/\text{Cu}/\text{PAN-C}$ ($0.109 \text{ cm}^3 \text{ g}^{-1}$) are smaller than

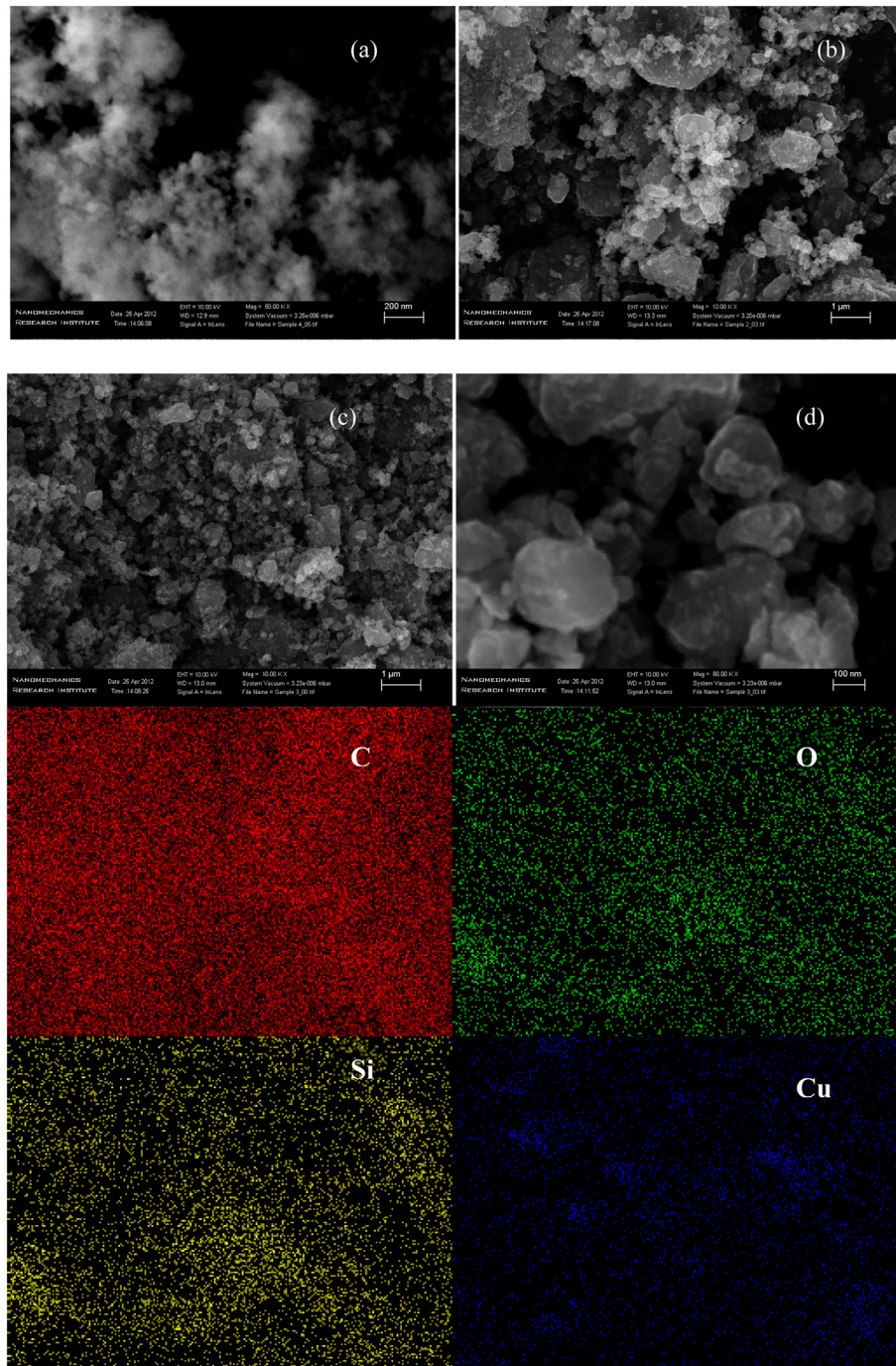


Fig. 3. SEM images of pure SiO_2 (a), $\text{SiO}_2/\text{PAN-C}$ (b) and $\text{SiO}_2/\text{Cu}/\text{PAN-C}$ (c) ((d) is magnification of (c)), and elemental maps in $\text{SiO}_2/\text{Cu}/\text{PAN-C}$.

those of $\text{SiO}_2/\text{PAN-C}$ ($0.123 \text{ cm}^2 \text{ g}^{-1}$). For the same reason, after the insertion of Cu, the BET surface area decreases from $73.8 - 51.6 \text{ m}^2 \text{ g}^{-1}$.

Fig. 5 displays the CV curves of $\text{SiO}_2/\text{Cu}/\text{PAN-C}$ at a scanning rate of 0.01 mV s^{-1} . In the first scanning cycle, there are one broad reduction peak located at 0.75 V , which disappears from the second cycle, and a wide cathodic peak in the range of $0.25-0 \text{ V}$. This cathodic peak at 0.75 V could be attributed to the formation of a SEI layer on the surface of the $\text{SiO}_2/\text{Cu}/\text{PAN-C}$ electrode [24]. The strong cathodic peak in the range of $0.25-0 \text{ V}$ should be assigned to the electrochemical reduction of SiO_2 (See Fig. 7) and the insertion of lithium into active materials, including Si and carbon. A broad

cathodic peak at 0.12 V and a broad anodic peak at 0.42 V gradually evolve from the first scanning cycle, and become more distinct in subsequent cycles, which correspond to the insertion/extraction reaction of lithium ions into/from the reduced Si, respectively.

Fig. 6(a) is the discharge–charge profile of $\text{SiO}_2/\text{Cu}/\text{PAN-C}$ at first two cycles at a constant current density of 55 mA g^{-1} . The discharge and charge specific capacities of $\text{SiO}_2/\text{Cu}/\text{PAN-C}$ at the 1st cycle are 902 and 651 mAh g^{-1} , respectively, which are much higher than carbonaceous materials. Clearly, the extra capacity comes from SiO_2 particles in the composite. This means that the reversible specific capacity of SiO_2 in the composite is $\sim 1230 \text{ mAh g}^{-1}$ ($300 * 0.53$ (for PAN-C) + $1230 * 0.40$ (for SiO_2) = 651 mAh g^{-1} (for the composite)),

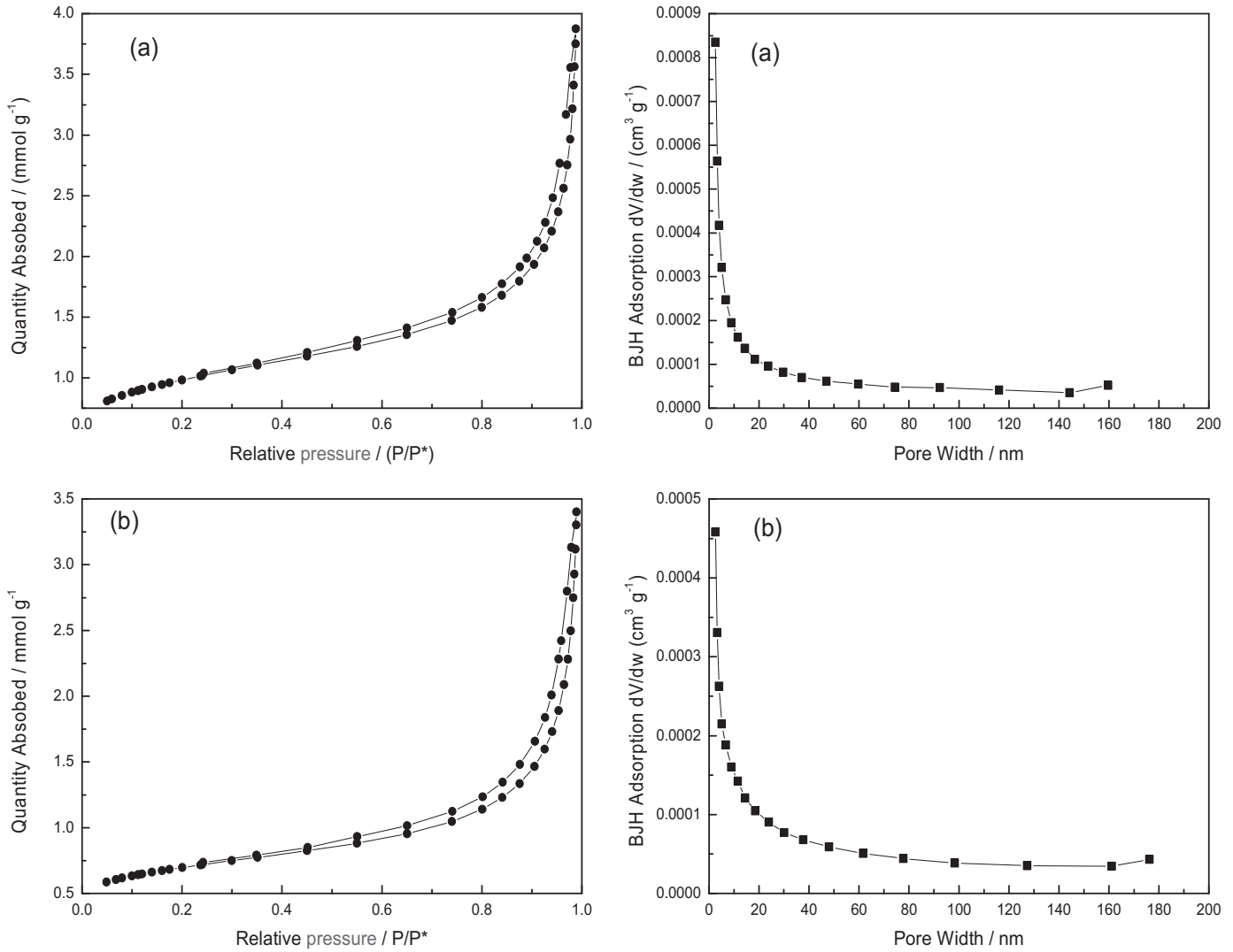


Fig. 4. BET isotherms and pore size distribution of SiO₂/PAN-C (a) and SiO₂/Cu/PAN-C (b).

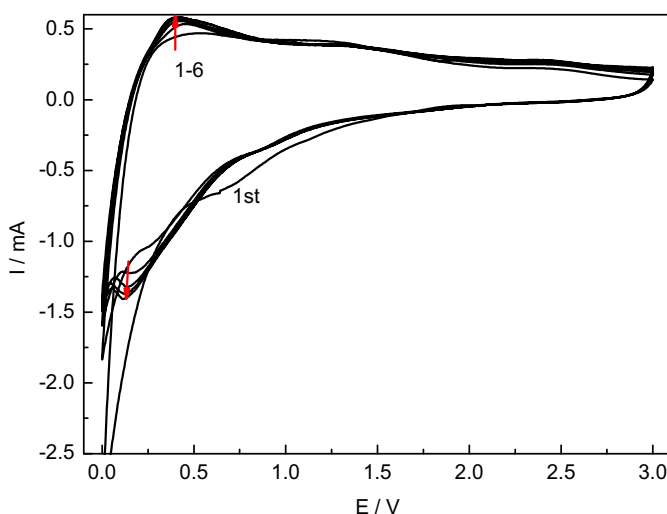


Fig. 5. Cyclic voltammogram curves of SiO₂/Cu/PAN-C at a scanning rate of 0.1 mV s⁻¹.

indicating that nano-SiO₂ is a promising lithium storage material. At the second cycle, the discharge specific capacity is 653 mAh g⁻¹ and the coulombic efficiency increases to 96.3% from 72.2% at the first cycle. There are two plateaus at ~0.75 V and 0.25–0.0 V in the first discharge curve, corresponding to the two anodic peaks in the cyclic voltammogram in Fig. 5. The plateau at about 0.75 V is associated with the electrolyte decomposition and the formation of the solid electrolyte interface (SEI) layer, which contributes about 150 mAh g⁻¹ to the total irreversible capacity of the cell (~251 mAh g⁻¹). Another plateau at less than 0.25 V is related to electrochemical reactions between lithium ions and active materials in the composite. In contrast, the discharge specific capacity and coulombic efficiency of SiO₂/PAN-C at the 1st cycle, which are 782 mAh g⁻¹ and 51.4%, respectively, are much less than those of SiO₂/Cu/PAN-C. Considering that the specific area of SiO₂/Cu/PAN-C is less than that of SiO₂/PAN-C, their discharge capacity difference should be attributed to a higher SiO₂ utilization percentage of SiO₂/Cu/PAN-C than SiO₂/PAN-C during the alloying/dealloying with Li. These results suggest that the addition of Cu significantly improves the electrochemical performance of SiO₂ composite materials.

In order to investigate the reaction mechanism of SiO₂ with lithium, XRD was used to examine the SiO₂/Cu/PAN-C electrode at

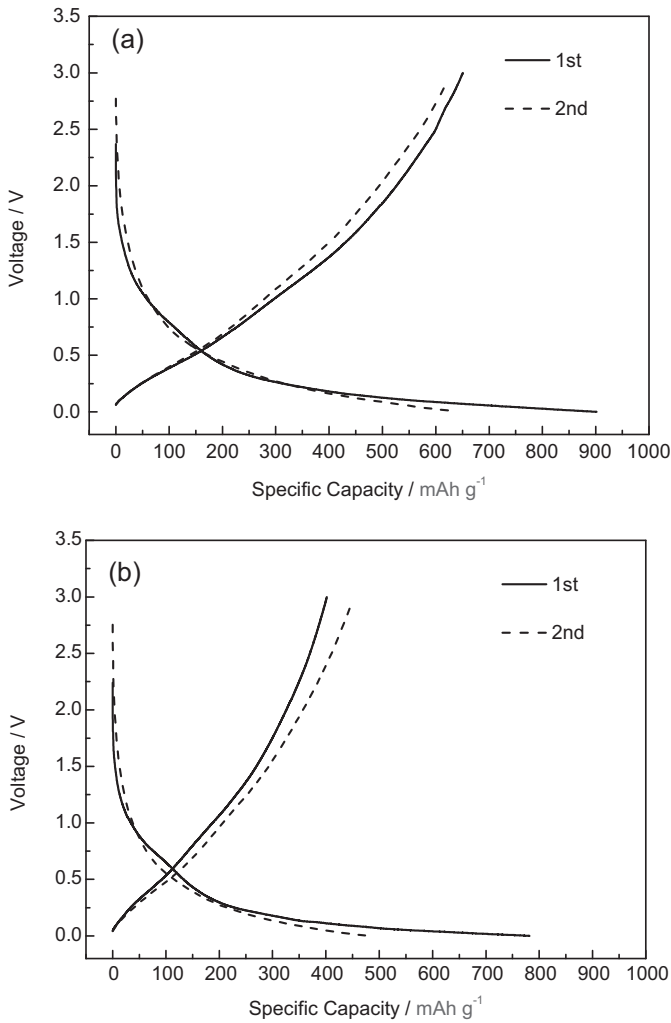


Fig. 6. Discharge–charge profile $\text{SiO}_2/\text{Cu}/\text{PAN-C}$ (a) and $\text{SiO}_2/\text{PAN-C}$ (b) at a constant current density of 55 mA g^{-1} .

different lithium insertion stages and after full lithium extraction in an ultrahigh purity argon atmosphere (Fig. 7). It can be found that this electrochemical reaction involves amorphous nano- SiO_2 being reduced and forming Li_2O , Li_4SiO_4 and $\text{Li}_2\text{Si}_2\text{O}_5$. When the electrode is discharged to 0.25 V, the characteristic peaks of Li_2O , Li_4SiO_4 and $\text{Li}_2\text{Si}_2\text{O}_5$ are observed and retain even after electrode is charged to 3 V at a current density of 55 mA g^{-1} , indicating the formed Li_2O , Li_4SiO_4 and $\text{Li}_2\text{Si}_2\text{O}_5$ have no capacity contribution. There are some distinct differences in comparison to previous literatures. Chen et al. [24] found that Li_2O was amorphous, but our result clearly shows that Li_2O presents good crystal. In addition, Sohn et al. [12] reported that $\text{Li}_2\text{Si}_2\text{O}_5$ had capacity contribution, but in our work, the characteristic peak of $\text{Li}_2\text{Si}_2\text{O}_5$ has no change after charging, indicating that $\text{Li}_2\text{Si}_2\text{O}_5$ is inactive to lithium. Combining previous literatures [21,24], in this work, the reaction mechanism may be as follows.

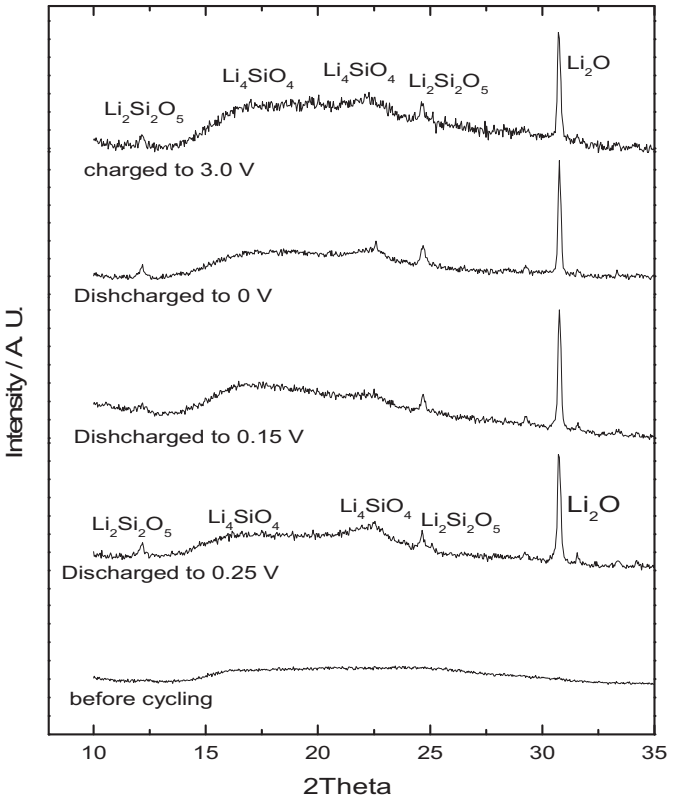
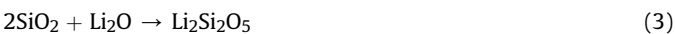


Fig. 7. XRD patterns of $\text{SiO}_2/\text{Cu}/\text{PAN-C}$ at different lithium insertion/extraction stages.

Reactions (1), (2) and (3) are irreversible. Supposing that the theoretical capacity of Si is about 3600 mAh g^{-1} at room temperature [28], the theoretical capacity of SiO_2 is $\sim 840 \text{ mAh g}^{-1}$ if it is reduced by way of reaction (1) alone, while the theoretical capacity of SiO_2 is about 1680 mAh g^{-1} if it is reduced by way of reaction (2) alone. In our work, the reversible specific capacity of SiO_2 in $\text{SiO}_2/\text{Cu}/\text{PAN-C}$ is about 1230 mAh g^{-1} . Clearly, the reactions (1) and (2) are simultaneous but reaction (2) is dominant.

Fig. 8 presents the cycling performance of $\text{SiO}_2/\text{Cu}/\text{PAN-C}$ and $\text{SiO}_2/\text{PAN-C}$ at a constant current density of 55 mA g^{-1} and 110 mA g^{-1} , respectively. Additionally, the cyclic performance curve of the pure SiO_2 is also given in Fig. 8. The pristine SiO_2 electrode only delivers a specific capacity of $\sim 50 \text{ mAh g}^{-1}$ and its coulombic efficiency is unstable, which may result from poor interface contact between SiO_2 and carbon black. Considering a part of this capacity may come from conductor AB, the electrochemical activity of pristine SiO_2 to lithium is low. This phenomenon was also observed in Yu's work, in which nano- SiO_2 mixed with Super P delivered a large resistance with a small specific capacity [21]. In contrast, both $\text{SiO}_2/\text{Cu}/\text{PAN-C}$ and $\text{SiO}_2/\text{PAN-C}$ exhibit a relatively high capacity with excellent cyclic performance, indicating that PAN-C matrix can facilitate charge transfer and provide a stable structure to buffer the volume change of active material. The improved cyclic stability should be attributed to following factors: Firstly, nano-sized SiO_2 particles greatly decrease the volume changes from lithium ion insertion and extraction, and meanwhile inert Li_2O , Li_4SiO_4 and $\text{Li}_2\text{Si}_2\text{O}_5$ formed in the first discharge can support and disperse the active Si formed by reduction, and accommodate volume changes during cycling [12]. Secondly, the preparation methods used in our experiments largely enhance the dispersity of SiO_2 among PAN-C. Ball milling, which is considered to be an effective method to disperse nano-materials, uniformly disperses nano- SiO_2 in the PAN solution. The addition of ethanol makes PAN precipitate on the

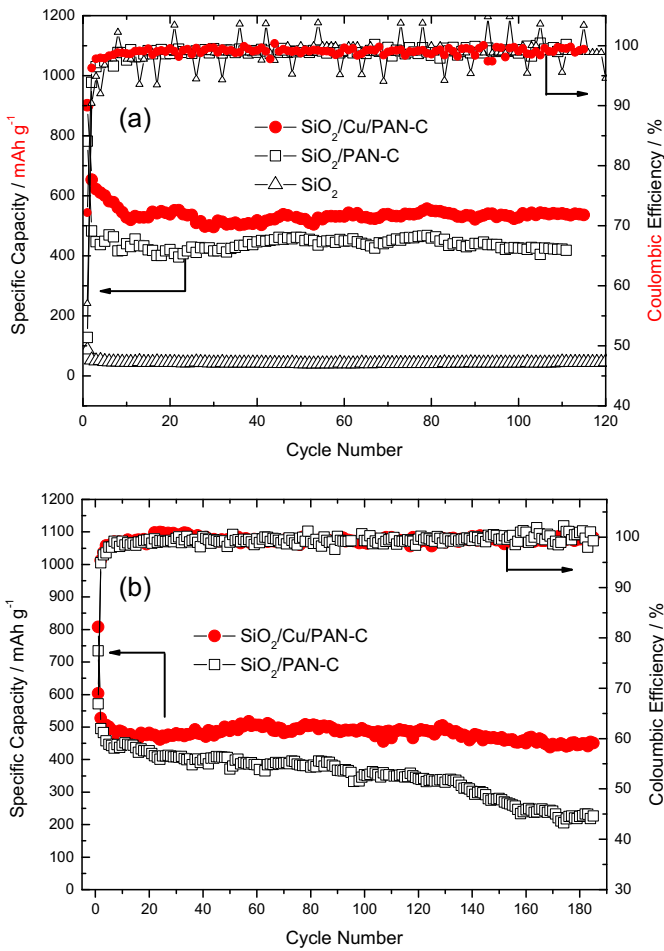
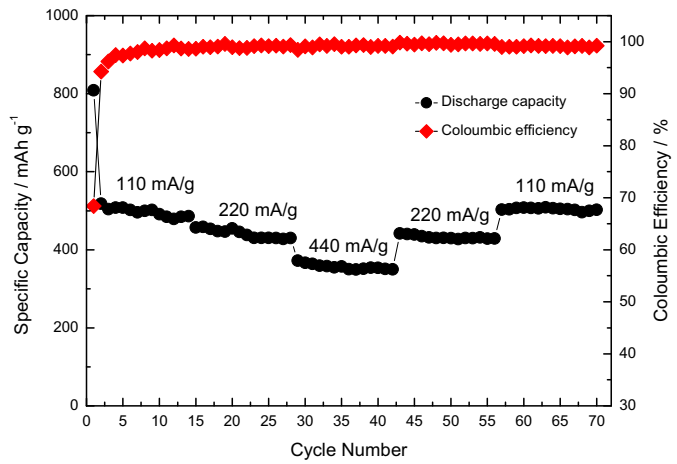


Fig. 8. Cycling performances of $\text{SiO}_2/\text{PAN-C}$ and $\text{SiO}_2/\text{Cu}/\text{PAN-C}$ at a constant current density of 55 mA g^{-1} (a) and 110 mA g^{-1} (b), respectively.

surface of SiO_2 rapidly, realizing the homogenous coating of SiO_2 by PAN. After pyrolysis, SiO_2 is homogeneously distributed in the PAN-C matrix, which prevents the local destruction of electrode microstructure during cycling. Thirdly, the porous structure of the resultant materials can better accommodate the volume variation of active material. Compared with $\text{SiO}_2/\text{PAN-C}$, $\text{SiO}_2/\text{Cu}/\text{PAN-C}$ presents higher specific capacity and better cyclic stability. At constant current density of 55 mA g^{-1} , $\text{SiO}_2/\text{Cu}/\text{PAN-C}$ exhibits a stable specific capacity of $\sim 537 \text{ mAh g}^{-1}$ after the 10th cycle with a capacity retention rate of 100% after the 115th cycle (Fig. 8(a)), while the stable specific capacity of $\text{SiO}_2/\text{PAN-C}$ is $\sim 430 \text{ mAh g}^{-1}$. At current density of 110 mA g^{-1} , there is a more obvious difference between them. The stable specific capacity of $\text{SiO}_2/\text{Cu}/\text{PAN-C}$ is $\sim 500 \text{ mAh g}^{-1}$ and 90% of the capacity is retained at the 185th cycle, while that of $\text{SiO}_2/\text{PAN-C}$ is $\sim 400 \text{ mAh g}^{-1}$ and begins to fade rapidly after 140 cycles (Fig. 8(b)). These results suggest that Cu can effectively improve the electrochemical properties of SiO_2 .

Fig. 9. Rate capability of $\text{SiO}_2/\text{Cu}/\text{PAN-C}$ composite.



plots of $\text{SiO}_2/\text{Cu}/\text{PAN-C}$ and $\text{SiO}_2/\text{PAN-C}$ before cycling and after different cycles. Before cycling, both electrodes show only one depressed semicircle in the high-frequency range and an inclined line in the low-frequency range. According to our previous study [29], the depressed semicircle diameter in the high-frequency

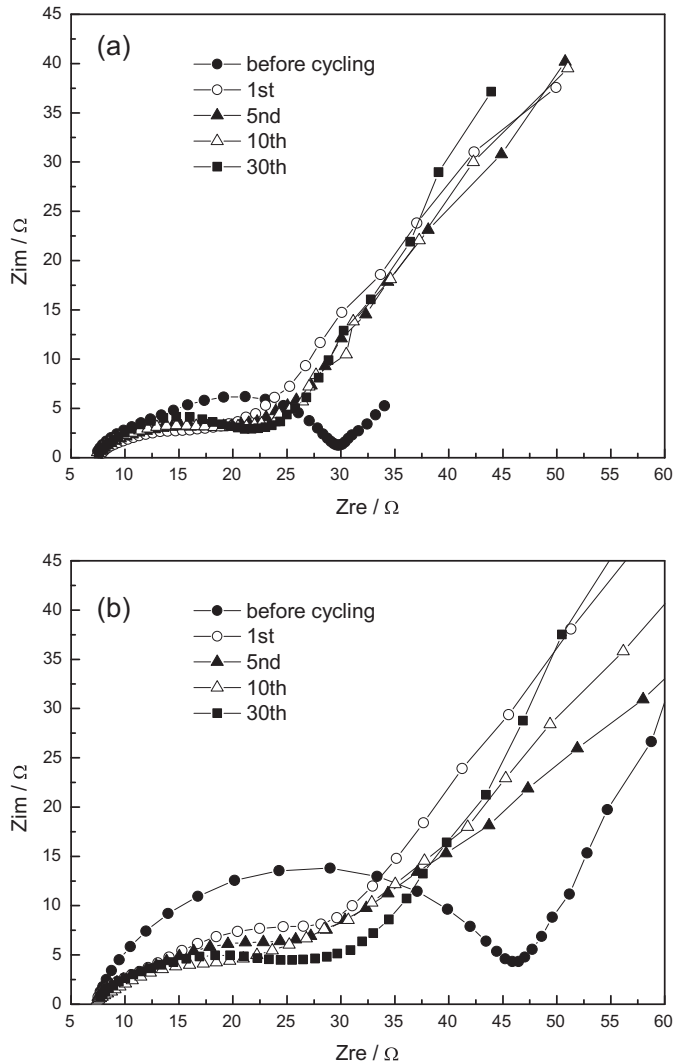


Fig. 10. Electrochemical impedance spectra of $\text{SiO}_2/\text{Cu}/\text{PAN-C}$ (a) and $\text{SiO}_2/\text{PAN-C}$ (b).

range represents the impedance of block electrodes, while the inclined line in the low-frequency region is attributed to the lithium ion diffusion impedance. From Fig. 10, with the addition of Cu, the resistance of electrode decreases from 45Ω to 30Ω . After cycling, both electrodes still show only a depressed semicircle, which means the overlap between the SEI film and the interfacial charge-transfer impedance. The $\text{SiO}_2/\text{Cu}/\text{PAN-C}$ electrode displays the resistance around 25Ω and negligible variance during 30 cycles, suggesting the stable interface impedance. However, the resistance of $\text{SiO}_2/\text{PAN-C}$ is about 35Ω . These results suggest that Cu can effectively enhance electric conductivity of the entire electrode and facilitate interfacial charge-transfer.

4. Conclusions

A new $\text{SiO}_2/\text{Cu}/\text{PAN-C}$ composite was synthesized by a simple method. At constant current density of 55 mA g^{-1} , the composite exhibits a stable specific capacity of $\sim 537 \text{ mAh g}^{-1}$ with a capacity retention rate of 100% after the 115th cycle. When current density increases to 440 mA g^{-1} , a stable capacity of $\sim 352 \text{ mAh g}^{-1}$ can be obtained. The improved electrochemical performance of the $\text{SiO}_2/\text{Cu}/\text{PAN-C}$ is attributed to the relatively little volume change of SiO_2 particles during cycling, the buffer effect of the formed inert matrix to volume change, the porous structure of the composite and the enhanced conductivity of the resultant electrode. The composite is a promising alternative anode material for lithium ion batteries.

Acknowledgments

This research was financially supported by Positec, the Natural Sciences and Engineering Research Council of Canada (NSERC), Canadian Foundation for Innovation (CFI) and the Canada Research Chairs (CRC) program.

References

- [1] M. Rao, W. Li, E.J. Cairns, *Electrochim Commun.* 17 (2012) 1–5.
- [2] M. Liu, C. Li, H. Du, X. You, *Chem. Commun.* 48 (2012) 4950–4952.
- [3] A.M. Chockla, K. Klavetter, C.B. Mullins, B.A. Korgel, *Chem. Mater.* 24 (2012) 3738–3745.
- [4] Z. Lu, J. Zhu, D. Sim, W. Shi, Y.Y. Tay, J. Ma, H.H. Hng, Q. Yan, *Electrochim. Acta* 74 (2012) 176–181.
- [5] W. Zhang, *J. Power Sources* 196 (2011) 13–24.
- [6] H. Chen, Y. Xiao, L. Wang, Y. Yang, *J. Power Sources* 196 (2011) 6657–6662.
- [7] Z. Zhou, Y. Xu, W. Liu, L. Niu, *J. Alloys Compd.* 493 (2010) 636–639.
- [8] C.K. Chan, H. Peng, G. Liu, K. Mcilwrath, X.F. Zhang, R.A. Huggins, Y. Cui, *Nat. Nanotechnol.* 3 (2008) 31–35.
- [9] X. Chen, X. Li, F. Ding, W. Xu, J. Xiao, Y. Cao, P. Meduri, J. Liu, G.L. Graff, J. Zhang, *Nano Lett.* 12 (2012) 4124–4130.
- [10] J. Hassoun, S. Panero, G. Mulas, B. Scrosati, *J. Power Sources* 171 (2007) 928–931.
- [11] K.H. Seng, M. Park, Z.P. Guo, H.K. Liu, J. Cho, *Angew. Chem. Int. Ed.* 51 (2012) 5657–5661.
- [12] W. Chang, C. Park, J. Kim, Y. Kim, G. Jeong, H. Sohn, *Energy Environ. Sci.* 5 (2012) 6895–6899.
- [13] Y. Zhao, X. Liu, H. Li, T. Zhai, H. Zhou, *Chem. Commun.* 48 (2012) 5079–5081.
- [14] N. Shin, M.A. Filler, *Nano Lett.* 12 (2012) 2865–2870.
- [15] M. Ge, J. Rong, X. Fang, C. Zhou, *Nano Lett.* 12 (2012) 2318–2323.
- [16] M. Saito, K. Nakai, T. Yamada, T. Takenaka, M. Hirota, A. Kamei, A. Tasaka, M. Inaba, *J. Power Sources* 196 (2011) 6637–6643.
- [17] J.R. Szczech, S. Jin, *Energy Environ. Sci.* 4 (2011) 56–72.
- [18] W. Wang, R. Epur, P.N. Kumta, *Electrochim. Commun.* 13 (2011) 429–432.
- [19] H. Wu, Y. Cui, *Nano Today* 7 (2012) 414–429.
- [20] U. Kasavajjula, C. Wang, A.J. Appleby, *J. Power Sources* 163 (2007) 1003–1039.
- [21] Y. Yao, J. Zhang, L. Xue, T. Huang, A. Yu, *J. Power Sources* 196 (2011) 10240–10243.
- [22] Y. Lu, Y. Wang, Y. Zou, Z. Jiao, B. Zhao, Y. He, M. Wu, *Electrochim. Commun.* 12 (2010) 101–105.
- [23] J. Lee, N. Choi, S. Park, *Energy Environ. Sci.* 5 (2012) 7878–7882.
- [24] B. Guo, J. Shu, Z. Wang, H. Yang, L. Shi, Y. Liu, L. Chen, *Electrochim. Commun.* 10 (2008) 1876–1878.
- [25] M.K. Datta, P.N. Kumta, *J. Power Sources* 158 (2006) 557–563.
- [26] Y. Liu, T. Chen, Y. Fu, M. Tse, J. Hsieh, P. Ho, Y. Liu, *J. Phys. D Appl. Phys.* 36 (2003) L97–L100.
- [27] J.C. Groen, L.A.A. Peffer, J. Pérez-Ramírez, *Microporous Mesoporous Mater.* 60 (2003) 1–17.
- [28] M.N. Obrovac, L.J. Krause, *J. Electrochim Soc.* 154 (2007) A103–A108.
- [29] M. Li, Z. Yu, X. He, *Electrochim. Acta* 55 (2010) 2217–2222.